This article has been accepted for publication in IEEE Transactions on Applied Superconductivity. This is the author's version which has not been fully edited and content may change prior to final publication. Citation information: DOI 10.1109/TASC.2025.3635639

From Modelling to Application: Exploring Quench Tolerance in High-Field HTS Magnets

Emily-Kei C. Brewerton *Member, IEEE*, Sriharsha Venuturumilli *Member, IEEE*, Jayani Karunarathna, Tom Simpson *Member, IEEE*, Konstantinos Bouloukakis, Theo Wordsworth, Rodney A. Badcock *Senior Member, IEEE*, Ratu C. Mataira

***Abstract*—In this work, a 2D axisymmetric FEM model was produced to simulate OpenStar Technologies' Junior Core Magnet. The model was created in COMSOL Multiphysics, with electromagnetic and thermal coupling. This model was used to simulate the Core Magnet under full-field conditions, and was verified against the specifications of the Core Magnet. Producing the model involved creating lookup tables of homogenised electrical and thermal properties for each of the 14 solder impregnated coils, applying coordinate transformations to these lookup tables, and creating 2D axisymmetric equivalent geometry of the complex copper interface buses and plates between the coils.**

This paper provides insight into understanding the behaviour of NI coils and how they influence quench dynamics, current redistribution, and thermal response. The modelling approach demonstrates that computationally efficient simulations can be achieved through homogenisation and geometry simplification, offering a valuable tool for the design, optimisation, and safety assessment of large-scale superconducting magnets.

***Index Terms*—Superconducting magnets, HTS, OpenStar Technologies, NI coils, FEM, quench.**

I. INTRODUCTION

HIGH temperature superconductors (HTS) are the most commonly used type in compact commercial fusion devices [1]. However, a superconducting magnet is susceptible to quenching [2, 3] which can cause a rise in the resistance of the material, and a further increase of temperature (due to Joule heating), creating a feedback loop that can lead to complete failure and breakdown of the magnet. As a result, being able to detect and prevent quenching is crucial to enable the development of nuclear fusion technologies. A quench in a magnet is one of the most challenging scenarios for any operator, often posing a serious risk to the magnet's integrity. HTS systems face unique challenges, including slow normal-zone propagation, and a wide operational temperature margin before superconductivity is lost. These factors hinder the effectiveness of conventional quench detection and protection strategies, especially in high-field environments. OpenStar Technologies' Junior Core Magnet [4] is a complex three-dimensional object, with many material components within its 14 solder-impregnated, non-insulated (NI) coils connected in series, as well as an intricate structural geometry - making it difficult to model.

In this work, a 2D axisymmetric finite element method (FEM) model of the Core Magnet was built in COMSOL Multiphysics [5] to model the electrical and thermal behaviour of the magnet, and was used to perform simulations to analyse the behaviour of the magnet leading up to forced quench events.

II. BUILDING THE MODEL

Building the FEM model involved three main steps. First, homogenizing the electrical and thermal properties of each of the 14 coils in the core magnet; second, applying coordinate transformations to these properties to account for the change from spiral to cylindrical coordinate systems when building a 2D axisymmetrical model; and third, creating equivalent 2D axisymmetric geometries of the copper interface plates and buses between the coils.

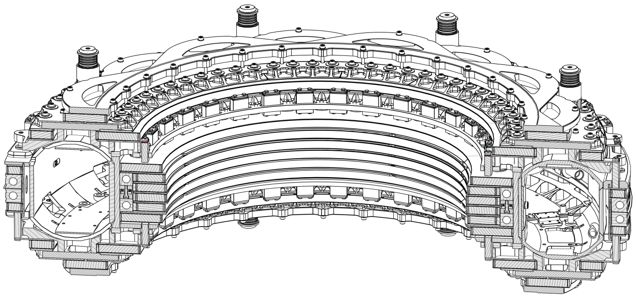

Fig. 1: CAD cross-section of OpenStar's Junior Core Magnet.

A. Coil Homogenization

Within each coil of the magnet, many layers of different materials are used, such as the solder, stainless steel tape, and HTS tape (which in itself is consisted of numerous different materials). These conductors are parallel-connected to form stacks, which are then wound to form single-pancake coils. As a result, the primary challenge faced by modellers in performing a detailed analysis of such a composite structure is that using a finite element mesh fine enough to capture the heterogeneous properties of each material in every turn of a coil, as well as their interactions with the entire structure, results in an excessively large number of degrees of freedom

---

This work was funded by OpenStar Technologies Ltd. (Corresponding author: Emily-Kei C. Brewerton)

Emily-Kei C. Brewerton, Sriharsha Venuturumilli, Jayani Karunarathna, Tom Simpson, Konstantinos Bouloukakis, Theo Wordsworth, Rodney A. Badcock and Ratu C. Mataira are with OpenStar Technologies, Wellington 6035, New Zealand. (e-mail: emily-kei.brewerton@openstar.nz). Rodney A. Badcock is also with Dodd-Walls Centre for Photonic and Quantum Technology, Lower Hutt 5046, New Zealand and Robinson Research Institute, Victoria University of Wellington, Lower Hutt 5046, New Zealand

[6]. This in turn directly impacts computation time, memory usage, and solver complexity due to an extremely large matrix of equations needed to be solved for. Homogenising the coils into one bulk material offers a practical trade-off, significantly reducing computational cost while preserving the essential electromagnetic and thermal behaviour of the structure.

Three physical properties of the coils were homogenized: electrical resistivity, thermal conductivity, and specific heat capacity. These are all temperature dependent, so lookup tables of the properties were produced to be implemented into the FEM model. For the Core Magnet, the HTS tapes used for the 14 coils are manufactured by Fujikura and Faraday Factory, and were assumed to consist of three layers, a Copper stabilizer (2×20 μm for Fujikura, 2×10 μm for Faraday Factory), a Hastelloy substrate (70 μm for Fujikura, 44 μm for Faraday Factory), and a REBCO superconducting layer that is only included for the electrical resistivity homogenizations (explained in section D).

Using the cross-section of a single turn of a coil, the thermal conductivities (κ) and electrical resistivities (ρ) were homogenized using combinations of thicknesses and widths of each material component (see Fig. 2a). The direction (r, ϕ, or z) determined whether the material properties were added in series, or in parallel to each other.

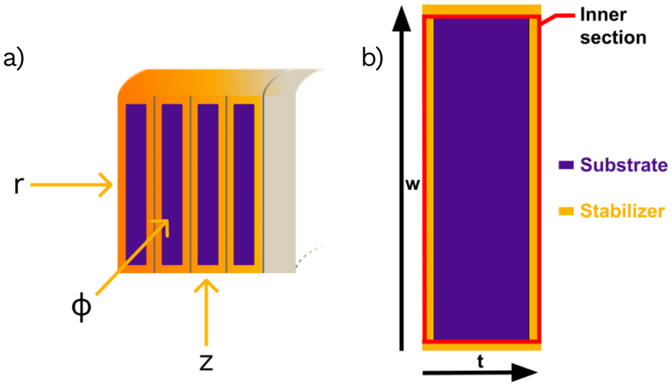

Fig. 2: a) One turn of a coil, with labelled directions needed to be calculated for the thermal conductivity and resistivity matrices. b) Cross-section of an HTS tape, highlighting the inner section that is homogenised first, where $w = 12$ mm, and $t = 110$ μm (Fujikura) or $t = 64$ μm (Faraday Factory).

For radial thermal conductivity component ($\kappa_{r'}$), the inner values (see Fig. 2b) are added in parallel, the outer values are added in series, and then the remaining values are added in parallel.

$$\kappa_{\text{inner}} = \left(\frac{1}{\kappa_{\text{Cu}}}\frac{t_{\text{Cu}}}{t_{\text{inner}}} + \frac{1}{\kappa_{\text{H}}}\frac{t_{\text{H}}}{t_{\text{inner}}}\right)^{-1} \tag{1a}$$

$$\kappa_{\text{HTS}} = \frac{w_{\text{inner}}\kappa_{\text{inner}} + w_{\text{outer}}\kappa_{\text{outer}}}{w_{\text{HTS}}} \tag{1b}$$

$$\kappa_{r'} = \left(\frac{1}{\kappa_{\text{HTS}}}\frac{t_{\text{HTS}}}{t_{\text{coil}}} + \frac{1}{\kappa_{\text{SS}}}\frac{t_{\text{SS}}}{t_{\text{coil}}} + \frac{1}{\kappa_{\text{solder}}}\frac{t_{\text{solder}}}{t_{\text{coil}}}\right)^{-1} \tag{1c}$$

Where t and w are the thicknesses and widths of the materials respectively, Cu represents the copper stabilizer, H represents the Hastelloy substrate, HTS and SS represent the HTS and stainless steel co-wound tapes respectively, and $solder$ represents the solder layers in-between each tape.

For thermal conductivity in the axial direction ($\kappa_{z'}$), the inner values are added in series, the outer values are added in parallel, and then the remaining values are added in series.

$$\kappa_{\text{inner}} = \frac{t_{\text{Cu}}\kappa_{\text{Cu}} + t_{\text{H}}\kappa_{\text{H}}}{t_{\text{inner}}} \tag{2a}$$

$$\kappa_{\text{HTS}} = \left(\frac{1}{\kappa_{\text{inner}}}\frac{w_{\text{inner}}}{w_{\text{HTS}}} + \frac{1}{\kappa_{\text{outer}}}\frac{w_{\text{outer}}}{w_{\text{HTS}}}\right)^{-1} \tag{2b}$$

$$\kappa_{z'} = \frac{t_{\text{HTS}}\kappa_{\text{HTS}} + t_{\text{SS}}\kappa_{\text{SS}} + t_{\text{solder}}\kappa_{\text{solder}}}{t_{\text{coil}}} \tag{2c}$$

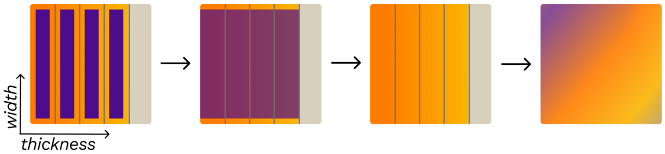

Fig. 3: Visual representation of the three simplification steps taken during the homogenization of the non-superconducting components in one turn of a coil.

For thermal conductivity in the azimuthal direction ($\kappa_{\phi'}$), as well as the homogenised specific heat capacities of the coils, the cross-sectional areas can be used: $A = w \times t$.

$$k_{\phi'} = \frac{A_{\text{Cu}}k_{\text{Cu}} + A_{\text{H}}k_{\text{H}} + A_{\text{SS}}A_{\text{SS}} + A_{\text{solder}}k_{\text{solder}}}{A_{\text{coil}}} \tag{3}$$

$$C_{\text{total}} = \frac{A_{\text{Cu}}C_{\text{Cu}} + A_{\text{H}}C_{\text{H}} + A_{\text{SS}}C_{\text{SS}} + A_{\text{solder}}C_{\text{solder}}}{A_{\text{coil}}} \tag{4}$$

For the electrical resistivity components, values are combined in the reverse manner of thermal conductivity. For example, where thermal conductivities are added in series, electrical resistivities are added in parallel. However, the homogenisation was only performed for $\rho_{\phi'}$. The $\rho_{r'}$ component was evaluated using a separate model, by matching the resultant radial resistance for a given resistivity to the tested radial resistances of each coil at 77 K. Then, this was extrapolated to obtain the lookup table with respect to temperature. For $\rho_{z'}$, an arbitrary value of 1 Ωm is applied. This value is chosen to reduce computation time, and does not significantly affect the results within the tested range.

B. Coordinate Transformations

NI coils are wound in a spiral shape, with N number of turns. However the 2D axisymmetric model depicts the coils as N concentric rings. In order to have an accurate representation of the thermal and electrical properties of the coils, a coordinate transform was applied to the thermal conductivity and electrical resistivity tensors - converting from the local spiral coordinate system (r', ϕ', z') to the global cylindrical coordinate system (r, ϕ, z). This transform was proposed by Mataira *et al* [7], and has been validated for electrical resistivity. The work in this paper extends this

This article has been accepted for publication in IEEE Transactions on Applied Superconductivity. This is the author's version which has not been fully edited and content may change prior to final publication. Citation information: DOI 10.1109/TASC.2025.3635639

concept, and applies the transform to the thermal conductivity of the coil, as well as the electrical resistivity. In this case, the axial components of both coordinate systems are equivalent, so z' will be referred to as z from here, and the transformation only affects the in-plane $r' - \phi'$ components.

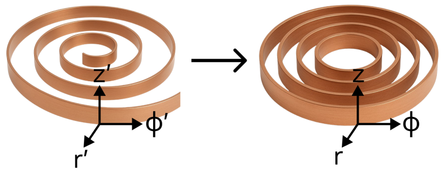

Fig. 4: Visualisation of the spiral winding of an HTS coil, and the concentric approximation used in a 2D axisymmetric model - with exaggerated spacing between turns.

The relationship between the spiral and cylindrical coordinate systems is determined using the small angle of deviation, α, formed between the orientation of the spiral winding, ϕ' and the azimuthal direction, ϕ [8]:

$$\alpha = \pm \sin^{-1}\left(\frac{d}{2\pi r}\right) \approx \frac{d}{2\pi r} \quad \text{as} \quad \frac{d}{r} \to 0 \tag{5}$$

Here, d is the thickness of one turn of the coil. In local spiral coordinates:

$$\vec{E}' = \boldsymbol{\rho}'\vec{J}' \quad \text{and} \quad \vec{q}' = -\boldsymbol{\kappa}'\nabla\vec{T}' \tag{6}$$

Where $\vec{E}'$ is the electric field, $\vec{J}'$ is the current density, $\vec{q}'$ is the heat flux, and $\nabla\vec{T}'$ is the temperature gradient. The anisotropic electrical resistivity and thermal conductivity tensors in local coordinates are:

$$\boldsymbol{\rho}' = \begin{bmatrix} \rho_{r'} & 0 & 0 \\ 0 & \rho_{\phi'} & 0 \\ 0 & 0 & \rho_z \end{bmatrix}_{\hat{r}',\hat{\phi}',\hat{z}} \qquad \boldsymbol{\kappa}' = \begin{bmatrix} \kappa_{r'} & 0 & 0 \\ 0 & \kappa_{\phi'} & 0 \\ 0 & 0 & \kappa_z \end{bmatrix}_{\hat{r}',\hat{\phi}',\hat{z}} \tag{7}$$

Rotating these tensors from the spiral coordinate system to the cylindrical coordinate system is done as follows [7]:

$$\vec{E} = g\vec{E}' = g\boldsymbol{\rho}'\vec{J}' = g\boldsymbol{\rho}'\left(g^{-1}\vec{J}\right) \tag{8a}$$

$$\vec{q} = g\vec{q}' = -g\boldsymbol{\kappa}'\nabla\vec{T}' = -g\boldsymbol{\kappa}'\left(g^{-1}\nabla\vec{T}\right) \tag{8b}$$

$$\implies \boldsymbol{\rho} = g\boldsymbol{\rho}'g^{-1} \quad \text{and} \quad \boldsymbol{\kappa} = g\boldsymbol{\kappa}'g^{-1} \tag{9}$$

Where g is the rotation matrix dependent on α:

$$g = \begin{bmatrix} \cos\alpha & -\sin\alpha & 0 \\ \sin\alpha & \cos\alpha & 0 \\ 0 & 0 & 1 \end{bmatrix} \tag{10}$$

Hence the electrical resistivity and thermal conductivity tensors in global cylindrical coordinates are given as:

$$\boldsymbol{\rho} = \begin{bmatrix} \rho_{rr} & \rho_{r\phi} & 0 \\ \rho_{\phi r} & \rho_{\phi\phi} & 0 \\ 0 & 0 & \rho_z \end{bmatrix}_{\hat{r},\hat{\phi},\hat{z}} \qquad \boldsymbol{\kappa} = \begin{bmatrix} \kappa_{rr} & \kappa_{r\phi} & 0 \\ \kappa_{\phi r} & \kappa_{\phi\phi} & 0 \\ 0 & 0 & \kappa_z \end{bmatrix}_{\hat{r},\hat{\phi},\hat{z}} \tag{11}$$

Where the components for the resistivity tensor are:

$$\rho_{rr} = \rho_r\cos^2\alpha + \rho_\phi\sin^2\alpha \tag{12a}$$

$$\rho_{r\phi} = \rho_{\phi r} = \frac{1}{2}(\rho_r - \rho_\phi)\sin 2\alpha \tag{12b}$$

$$\rho_{\phi\phi} = \rho_\phi\cos^2\alpha + \rho_r\sin^2\alpha \tag{12c}$$

The components for thermal conductivity are in the same form.

C. 2D Axisymmetric Geometries

Due to the axisymmetric nature of the 14 coils, these were represented as rectangles with equivalent width and height in the FEM model. However, the copper plates and buses that connect the coils are much more complex 3D objects, and are not axisymmetric around the z-axis, as shown in Fig. 5.

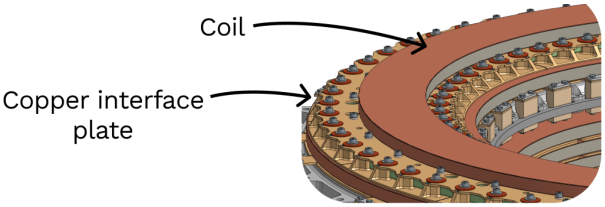

Fig. 5: Section of the Core Magnet CAD, showing one of the copper plates that connect the coils.

As a result, simplification of these copper plates was needed, without changing their final volumes. This was done by repeatedly creating horizontal ‘slices’ in the x-y plane of the CAD files of the interface plates, with increasing height of 1 mm increments, and measuring the cross-sectional areas of these slices. These measured areas for each interface plate were then substituted into the formula for the area, A of a ring:

$$A = 2\pi(R_2^2 - R_1^2) \tag{13}$$

Where R_1 and R_2 are the inner and outer radii of the ring, respectively. Then, by defining either R_1 or R_2 so that it forms a straight line with changing height in the z-direction, the other radius can be found. These two R values were used as the r coordinates for the copper interface plates in the FEM model. This method of producing 2D axisymmetric equivalent geometries enables accurate modelling of conductive heat transfer, as the heat transfer rate is dependent on both the surface area and the conduction length. Preserving the volumes of the copper plates also ensures their heat capacities remain unchanged, as these scale with volume.

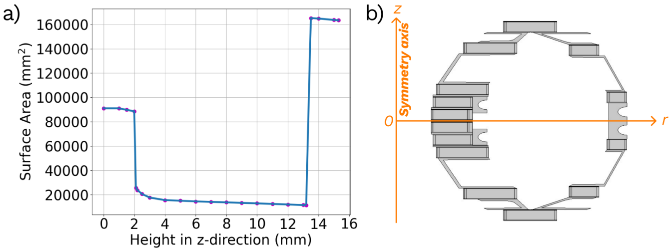

Fig. 6: a) Example of measured surface area data with changing height in the z-direction. b) Final 2D axisymmetric geometry of the Junior magnet.

D. COMSOL Set-up

The final geometry of the model is shown in Fig. 6b, which includes the 14 coils, each with bobbins and terminal plates, copper interface plates, and heat exchangers. When meshing the coils, the mesh number along the thickness of the coil was made to be equal to the number of turns [8]. The simulation involves coupled electromagnetic and thermal analyses. The electromagnetic study uses the *H*-formulation approach, while the thermal study uses the heat transfer through solids module. The governing equations are:

$$\mathbf{J} = \nabla \times \mathbf{H} \tag{14a}$$

$$\nabla \times \mathbf{E} = -\frac{\partial \mathbf{B}}{\partial t} \tag{14b}$$

$$\varrho C_p \frac{\partial T}{\partial t} + \nabla \cdot \mathbf{q} = Q \tag{15a}$$

$$\mathbf{q} = -\kappa \nabla T \tag{15b}$$

In Eqs. (14a)–(14b), $\mathbf{J}$ and $\mathbf{H}$ are the current density and magnetic field, respectively. $\mathbf{E}$ is the electric field, and $\mathbf{B}$ is the magnetic flux density. In Eqs. (15a)–(15b), ϱ is the density, C_p the specific heat capacity, T the temperature, $\mathbf{q}$ the heat flux, κ the thermal conductivity, and Q the volumetric heat source.

The $E-J$ power law is the non-linear relationship used for the superconducting properties of HTS tape [7, 9, 10], and is integrated into the FEM model by defining the resistivity of the REBCO material as follows:

$$\rho_{sc} = \frac{E_0}{J_c(B,\theta)} \left| \frac{J_t}{J_c(B,\theta)} \right|^{n-1} \tag{16}$$

Where $E_0 = 1\mu V$/cm is the electric field criterion for critical current, $n = 20$ is the flux-flow component, and $J_c(B,\theta)$ is the field-dependent critical current density taken as a 3D look-up table from the Robinson HTS Wire Critical Current Database [8, 9, 11]. J_t is the spiral current density in each coil:

$$J_t = J_\phi \cos\alpha + J_r \sin\alpha \tag{17}$$

Then, the total azimuthal resistivity of each coil is defined as:

$$\rho_{\phi' \text{ total}} = \left(\frac{1}{\rho_{\phi'}} + \frac{1}{\rho_{sc}} \right)^{-1} \tag{18}$$

$\rho_{\phi'}$ is the homogenised resistivity component equivalent to $\kappa_{\phi'}$ from Eqn. 3.

III. Results and Discussion

A. Initial Simulation

An initial simulation was set-up to mimic the experimental conditions of charging the Core Magnet to full field (5.6 T). This was done by charging the magnet up to 1440 A at a rate of 1 A/min, with the temperature fixed at 50 K and the electrical pathway shown in Fig. 7a (with the source current applied to Coil 7A first). The source current was then held constant for 20 hours, before a "sudden discharge" was performed by switching off the source current, as well as the fixed temperature. The model simulated a further 15 hours to analyse the discharge and heat-up of the magnet.

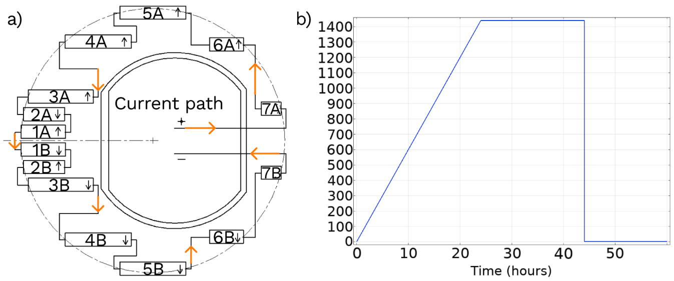

Fig. 7: a) Visualization of the electrical pathway through the series-connected coils in the Junior magnet. b) Source current (A) applied to the simulation.

The maximum B field is measured to be 5.8 T (see Fig. 8a). This is within 4% of the expected maximum field of Junior. It is also observed that there is almost zero B field in the space within the coils. This is the Zero-Field Region of the magnet, where the HTS flux pump and electronics are placed to power the magnet while it levitates.

A snapshot of the azimuthal current distribution throughout the magnet while the source current is ramped-up is shown in Fig. 8b. The outer coils of Junior are observed to experience screening current effects from the inner coils. This is due to them having smaller radial resistances and hence larger time constants than the inner coils. These screening currents may, in reality, induce additional mechanical stresses within the coils and potentially influence their superconducting performance. However, such effects are neglected in this particular model.

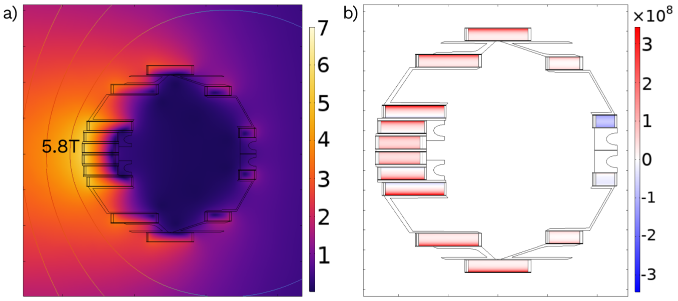

Fig. 8: a) Maximum magnetic field results, units Tesla. b) Snapshot of magnet current density during current ramp, showing screening current effects.

The homogenised specific heat capacities of each of the coils, along with the specific heat capacity of copper, were used to calculate the total heat capacity of the magnet. Then, by integrating this with respect to temperature, the total enthalpy of the magnet was plotted, as shown in Fig. 9a. Junior is expected to have a stored energy of 0.55 MJ. Assuming all this stored energy is dissipated into the magnet as heat, the resultant temperature change is predicted to be 16.5 K, (reaching 66.5 K from an initial temperature of 50 K). The simulation results show that the final surface temperature across the model is 67.0 K (17 K temperature change), placing the predicted and simulated change within 3% of each other. This result is used as justification that the model is correctly converting the stored energy from charging into heat, and that the magnet is not dissipating energy into the surroundings.

This article has been accepted for publication in IEEE Transactions on Applied Superconductivity. This is the author's version which has not been fully edited and content may change prior to final publication. Citation information: DOI 10.1109/TASC.2025.3635639

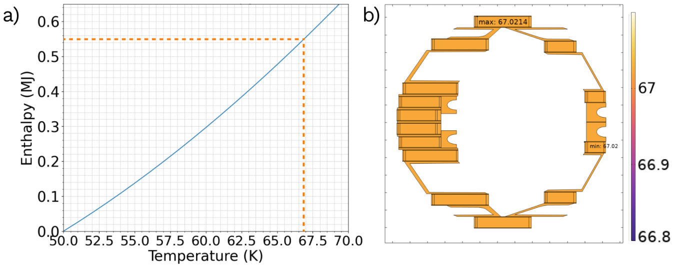

Fig. 9: a) Calculated total enthalpy of the magnet with respect to temperature when the initial temperature is 50 K. b) Final surface temperature after magnet discharges.

In analysing the sudden discharge results, no quench was observed within the 2D axisymmetric model. The temperature rise was uniform and the azimuthal currents through each of the coils remained below the critical current of the HTS tape, indicating that the magnet's no-insulation design and thermal capacity allow it to absorb the full stored energy without localised transitions.

B. Quench Simulations

A quench event was simulated by creating a local defect in Coil 4A (see Fig. 10a), by degrading the critical current I_c by 50% in two of the turns. Then, similarly to the last simulation, the magnet was ramped up to 1440 A and then held steady for 10 hours at a fixed temperature of 50 K, before simulating the cryocooler switching off while maintaining full-field current - allowing the magnet to heat up. The voltage across the magnet is defined as the potential difference obtained by integrating the electric field between the current terminals of the full coil assembly. This corresponds to the measurable terminal voltage that would be observed experimentally. In this work, the quench point refers to the first point at which the gradient of this voltage is largest.

Leading up to the quench event, an increasing temperature gradient is observed across the magnet, shown in Fig. 10b - with the maximum $\Delta T = 4.5$ K at the point of quench. This is likely due to the tested radial resistances of the magnet being larger on the inner coils compared to the outer coils. This gives us a clear indication that the inner coils are more prone to localised heating during current redistribution, making them the most likely initiation point for a quench event.

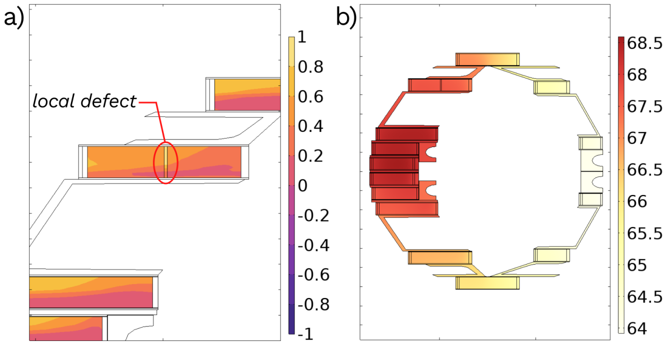

Fig. 10: a) Zoomed-in section of γ (gamma) surface plot during charging, showing the local defect in one of the coils. b) Surface temperature plot at quench point.

As expected, while the magnet was charging, $\gamma = \frac{J_t}{J_c}$ was observed to be significantly higher in the local-defect section of the coil. This can be seen in Fig. 10a. After the cryocooler is turned off, the temperature begins to increase, and consequently, γ also increases in each of the coils.

Looking at the voltage drop across the magnet, the quench event occurs at 1.805e5 s $\approx$ 6.2 hours after the cryocooler was turned off, as shown in Fig. 11.

The slow behaviour of the magnet observed in both simulations is due to the NI coils having turn-to-turn electrical contact, allowing current to redistribute radially across turns. This inherent current sharing introduces significant time constants into the system, leading to gradual changes in the magnetic field and therefore energy dissipation, rather than rapid transients.

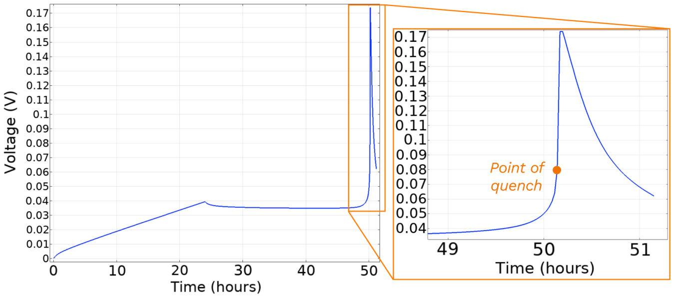

Fig. 11: Voltage across the magnet with time, with an inset showing the point of quench in the magnet. Note: the linear resistance seen on current ramp arises due to the combination of turn-turn resistance from the homogenized resistivities of each coil (contact resistance is inherent in the measured radial resistivities used).

IV. CONCLUSION

A 2D axisymmetric FEM model of OpenStar's Junior Magnet was successfully developed, accurately capturing the magnet's coupled electrical and thermal behaviour. Using this model, the magnet was then shown to be quench tolerant under "sudden discharge" conditions, and initial quench simulations were performed, providing increased confidence in our understanding of the system. While these results highlight key trends in quench development, the 2D axisymmetric approach cannot determine the exact initiation points of quenching; a full 3D model would be required for that level of spatial accuracy. The effects of solder voids, local defects in the HTS tape, imperfect contacts, and other manufacturing imperfections remain to be investigated, ideally supported by targeted experimental studies. The work in this paper serves as a strong foundation for future predictive modelling, including post-quench behaviour and structural–mechanical coupling.

REFERENCES

[1] Pierluigi Bruzzone et al. "High temperature superconductors for fusion magnets". In: *Nuclear Fusion* 58 (10 2018), p. 103001. ISSN: 0029-5515. DOI: 10.1088/1741-4326/aad835.

This article has been accepted for publication in IEEE Transactions on Applied Superconductivity. This is the author's version which has not been fully edited and content may change prior to final publication. Citation information: DOI 10.1109/TASC.2025.3635639

[2] Maxim Marchevsky. "Quench detection and protection for high-temperature superconductor accelerator magnets". In: *Instruments* 5 (3 Sept. 2021). ISSN: 2410390X. DOI: 10.3390/INSTRUMENTS5030027.

[3] Yawei Wang et al. "Quench behavior of high-temperature superconductor (RE)Ba2Cu3Ox CORC cable". In: *Journal of Physics D: Applied Physics* 52 (34 June 2019). ISSN: 13616463. DOI: 10.1088/1361-6463/ab1e2c.

[4] Craig S. Chisholm et al. *Design and initial results from the "Junior" Levitated Dipole Experiment*. 2025. arXiv: `2508.17691 [physics.plasm-ph]`. URL: https://arxiv.org/abs/2508.17691.

[5] COMSOL Multiphysics. "Introduction to COMSOL multiphysics®". In: *COMSOL Multiphysics, Burlington, MA* 9 (1998), p. 2018.

[6] M Lefik and B. A Schrefler. "Application of the homogenisation method to the analysis of superconducting coils". In: *Fusion Engineering and Design* 24 (3 June 1994), pp. 231–255. ISSN: 0920-3796. DOI: 10.1016/0920-3796(94)90024-8.

[7] Ratu C Mataira et al. "Finite-element modelling of no-insulation HTS coils using rotated anisotropic resistivity". In: *Superconductor Science and Technology* 33 (June 2020), 08LT01. ISSN: 0953-2048. DOI: 10.1088/1361-6668/ab9688.

[8] Sriharsha Venuturumilli et al. "Modeling HTS non-insulated coils: A comparison between finite-element and distributed network models". In: *AIP Advances* 13 (Mar. 2023), p. 035317. ISSN: 2158-3226. DOI: 10.1063/5.0135291.

[9] Jeseok Bang. "A FEM Simulation Model to Calculate Local Currents and Voltages of NI REBCO Coil With Both Screening Current and Transverse Current Considered". In: *IEEE Transactions on Applied Superconductivity* 34 (6 Sept. 2024), pp. 1–7. ISSN: 1051-8223, 1558-2515, 2378-7074. DOI: 10.1109/TASC.2024.3409147.

[10] Leiwen Yue et al. "Investigate on the Electromagnetic and Loss Characteristics of NI HTS Multi-Pancake Coil During Charging Process". In: *IEEE Transactions on Magnetics* 61 (1 Jan. 2025), pp. 1–10. ISSN: 0018-9464, 1941-0069. DOI: 10.1109/TMAG.2024.3502443.

[11] Robinson Research Institute. *Robinson HTS Wire Critical Current Database*. Accessed: 2024-11-20. 2024. URL: https://htsdb.wimbush.eu/.